Annual Review of Physical Chemistry

Slow Photoelectron Velocity-Map Imaging of Cryogenically Cooled Anions

Marissa L. Weichman[1,2] and Daniel M. Neumark[1,3]

[1]Department of Chemistry, University of California, Berkeley, California 94720, USA; email: weichman@berkeley.edu, dneumark@berkeley.edu

[2]Current affiliation: JILA, National Institute of Standards and Technology, Boulder, Colorado 80305, USA

[3]Chemical Sciences Division, Lawrence Berkeley National Laboratory, Berkeley, California 94720, USA

Annu. Rev. Phys. Chem. 2018. 69:4.1–4.24

The *Annual Review of Physical Chemistry* is online at physchem.annualreviews.org

https://doi.org/10.1146/annurev-physchem-050317-020808

Keywords

anion photoelectron spectroscopy, high-resolution photoelectron imaging, velocity-map imaging, cryogenic cooling, vibronic structure, transition state spectroscopy

Abstract

Slow photoelectron velocity-map imaging spectroscopy of cryogenically cooled anions (cryo-SEVI) is a powerful technique for elucidating the vibrational and electronic structure of neutral radicals, clusters, and reaction transition states. SEVI is a high-resolution variant of anion photoelectron spectroscopy based on photoelectron imaging that yields spectra with energy resolution as high as 1–2 cm^{-1}. The preparation of cryogenically cold anions largely eliminates hot bands and dramatically narrows the rotational envelopes of spectral features, enabling the acquisition of well-resolved photoelectron spectra for complex and spectroscopically challenging species. We review the basis and history of the SEVI method, including recent experimental developments that have improved its resolution and versatility. We then survey recent SEVI studies to demonstrate the utility of this technique in the spectroscopy of aromatic radicals, metal and metal oxide clusters, nonadiabatic interactions between excited states of small molecules, and transition states of benchmark bimolecular reactions.

1. INTRODUCTION

EA: electron affinity

eBE: electron binding energy

eKE: electron kinetic energy

FC: Franck–Condon

Transient species lie at the heart of chemical reactivity and play a key role in almost all complex reaction mechanisms. In the gas phase, open-shell free radicals are important in combustion chemistry (1, 2), atmospheric chemistry (3, 4), and astrochemistry (5, 6). Heterogeneous chemistry on a bulk surface is catalyzed at reactive sites, and these sites can be modeled by considering the structure, spectroscopy, and reactivity of metal and metal oxide clusters (7, 8). Nonadiabatic molecular dynamics following photoexcitation of small molecules are inextricably linked to the vibronic structure of the involved excited states (9, 10). Transition states and weakly bound adducts along a reaction coordinate govern molecular behavior and reactivity at the most fundamental level (11, 12).

Anion photoelectron spectroscopy (PES) is a versatile tool for studying these unusual species (13–15). Nearly any neutral molecule or cluster can be probed with anion PES, provided that it has a positive electron affinity (EA) and the corresponding anion can be synthesized. These conditions are often satisfied for free radicals, making them an appealing target for anion PES (16–19). Low-lying electronic excited states of exotic neutral species are also easily probed. The ability to mass-select anions prior to spectroscopic interrogation also makes PES an excellent method for size-dependent cluster studies. The evolution of geometries, bonding motifs, electronic structure, and other properties can be tracked as a function of cluster size as one approaches the bulk limit (20–24). Finally, PES is also one of the few ways to spectroscopically probe neutral unimolecular and bimolecular reactive surfaces, through photodetachment of a bound anion similar in geometry to the desired neutral transition state (25, 26).

Experimentally, a packet of mass-selected molecular anions, A^-, is intersected with a laser beam. If the laser photon energy exceeds the binding energy of the electron to the anion, a photoelectron may be detached:

$$A^- + h\nu \rightarrow A + e^-. \quad 1.$$

The kinetic energy distribution of the nascent electrons is measured. This distribution can show discrete features corresponding to detachment to specific neutral electronic and vibrational quantum states. The energy given to the system by the photon ($h\nu$) must be conserved between overcoming the binding energy of the electron to a given neutral state (eBE) and the kinetic energy of the outgoing photoelectron after detachment (eKE):

$$\text{eBE} = h\nu - \text{eKE}. \quad 2.$$

The energetics of this process are shown schematically in **Figure 1**. Photoelectron spectra are typically plotted in eBE because this quantity is independent of the choice of photon energy. An anion PES experiment can directly yield the EA and energetics of the electronic and vibrational levels of the neutral. Photoelectron angular distributions (PADs), which report on the electronic symmetry of a photodetachment transition, can also be extracted.

Photoelectron spectroscopy has somewhat relaxed selection rules compared to bound-bound electronic spectroscopy because of the ability of the photoelectron to carry away whatever kinetic energy and angular momentum is necessary for a given transition. Any neutral state accessible by removal of an electron from an atomic or molecular orbital can be formed by photodetachment. There are thus no dipole-forbidden transitions, and with a single photon energy, transitions can be made to all allowed states lying lower in eBE than $h\nu$. Neutral states are accessible with spin multiplicity differing by ± 1 from that of the anion; for instance, both singlet and triplet neutral states are accessible from detachment of a doublet anion (27, 28).

Relative intensities of features in a photoelectron spectrum yield information about the difference in equilibrium geometries between the anionic and neutral states. The Franck–Condon (FC)

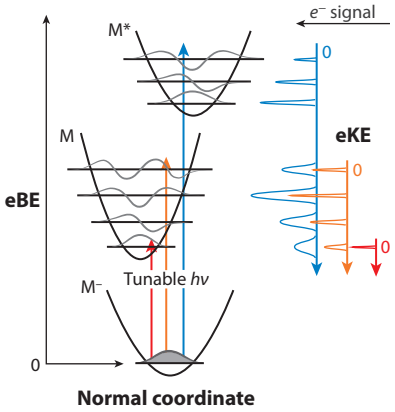

Figure 1

Energetic principles of slow photoelectron velocity-map imaging (SEVI) spectroscopy. A photoelectron is detached from the anion of interest using a tunable laser. The kinetic energy distribution of the resulting electrons (eKE) is analyzed using a velocity-map imaging spectrometer, yielding high energy resolution for the slowest electrons. Spectra are typically plotted in electron binding energy (eBE $= h\nu$ – eKE), which is independent of photon energy.

factor $|\langle\psi_v^f|\psi_v^i\rangle|^2$ governs the selection rules for vibrational transitions between initial and final states ψ_v^i and ψ_v^f and relative intensities of different transitions within an electronic band. Excitation occurs to neutral vibrational levels in accordance with their net overlap with the initial anion vibrational wavefunction. FC-allowed transitions can exhibit a change in vibrational quantum number of $\Delta v = 0, \pm1, \pm2...$ for totally symmetric vibrational modes and $\Delta v = 0, \pm2, \pm4...$ for nontotally symmetric modes. In practice, a large change in geometry between anion and neutral is associated with large FC factors for vibrational modes whose motion distorts the molecule along the displacement vector between anion and neutral equilibrium geometries. Nontotally symmetric FC-forbidden modes can also appear by borrowing intensity through Herzberg–Teller vibronic coupling to another electronic state (29, 30) or through resonant vibrational autodetachment mediated by an anion excited state (31).

In this article we review developments in slow photoelectron velocity-map imaging (SEVI) spectroscopy, a high-resolution variant of anion PES based on photoelectron imaging, and its recent applications to cryogenically cooled anions (cryo-SEVI). The functional utility of anion PES has historically been limited by the energy resolution of eKE detection and spectral congestion caused by warm molecular anions. With SEVI, photodetachment is carried out close to threshold and with selective detection of the slowest electrons, for which the energy resolution is best (32, 33). The flexibility and capability of this method are greatly enhanced by trapping and cryogenically cooling the anions prior to photodetachment, yielding spectra of complex molecular anions with energy resolution as high as 1–2 cm^{-1} (34). In the following sections, we cover the history, development, and technical details of SEVI spectroscopy. We then review several (cryo-)SEVI studies from both our laboratory and elsewhere to illustrate the versatility and capabilities of the technique.

Slow photoelectron velocity-map imaging of cryogenically cooled anions (cryo-SEVI): a high-resolution variant of anion photoelectron spectroscopy

2. A BRIEF HISTORY

The first anion PES experiment was reported by Hall and coworkers in 1967 (35) and was carried out with a continuous ion source, a continuous-wave (cw) intracavity argon ion laser, and

TOF: time of flight

VMI: velocity-map imaging

Zero electron kinetic energy (ZEKE) spectroscopy: a photoelectron spectroscopy variant where threshold electrons are detected as the wavelength is scanned

detection of the eKE distribution using a hemispherical energy analyzer. Even as other anion PES technologies were developed, the cw method has remained a workhorse technique and has been applied with great success by Lineberger, Ellison, Bowen, and others (13, 15, 21) to an extensive array of atoms, small molecules, clusters, and complexes.

The development of pulsed anion PES by Johnson and coworkers (36) and Smalley and coworkers (37) in the 1980s was spurred by the availability of shorter-wavelength and more flexible pulsed laser sources and an interest in anions more easily generated in pulsed free jet expansion sources. Initially, eKE distributions were measured via the time of flight (TOF) of the detached electrons, either field-free or using a magnetic bottle scheme (38). With the advent of ion imaging (39) and velocity-map imaging (VMI) (40) techniques, Sanov and others (41, 42) harnessed photoelectron imaging as an attractive PES alternative that combines high collection efficiency with the ability to detect low-eKE electrons and measure angular distributions. These pulsed techniques also made possible the development of pump–probe time-resolved anion PES to study ultrafast dynamics in small gas-phase molecules (43, 44).

The eKE resolution in anion PES is limited to about 50 cm^{-1} for the hemispherical analyzer (29), 40–80 cm^{-1} at best for conventional electron TOF (45), and about 150 cm^{-1} for magnetic bottle TOF (46). In photoelectron VMI, the energy resolution depends on the eKE of the detached photoelectrons, with $\Delta eKE/eKE \sim 3\%$ reported for the original Eppink–Parker design (40). These techniques are sufficient to measure electronic transitions, with vibrations resolved only in favorable systems with amenable FC structure. Resolution poses a particular barrier for species with low-frequency FC-active vibrations and in cases where warm ion temperatures lead to spectral congestion.

To improve the energy resolution of these experiments, the Neumark group adapted zero electron kinetic energy (ZEKE) spectroscopy, a technique developed by Müller-Dethlefs and coworkers (47, 48) for neutral molecules, to studies of negative ions. In anion ZEKE, the photon energy is scanned and only those electrons detached at threshold, with essentially zero eKE, are detected (49). This yielded resolution as high as 1–2 cm^{-1} for atomic anions. Molecular systems demonstrated more typical peak widths of $\sim$10 cm^{-1} because of rotational broadening (50).

However, anion ZEKE proved to be experimentally challenging and suitable only for a small fraction of systems. In ZEKE spectroscopy of neutrals, electrons are excited to high-lying Rydberg states and are pulsed-field ionized shortly before detection (51). Given the absence of Rydberg states in anions, the physics of anion ZEKE is quite different, and the collection of ZEKE electrons without distortion by stray fields is difficult. Additionally, photodetachment transitions of certain symmetries can suffer from poor threshold cross section and cannot be measured with ZEKE (52). Despite these limitations, ZEKE spectroscopy was applied to a number of molecular and cluster anions (53–57).

The photodetachment microscopy method of Blondel and coworkers (58, 59), where atomic anions are photodetached very close to threshold in the presence of an electric field, also warrants mention. The resulting photoelectrons are imaged in order to observe an interference pattern from which the eKE can be determined with great precision. This technique has been instrumental in measuring atomic EAs with great accuracy and has also been applied to OH and SH (60), but it appears to be less suited for studying more complex molecular systems and extended energy ranges.

The field thus remained open for a molecular photodetachment technique that could bridge the gap between the versatility and experimental simplicity of conventional anion PES and the high energy resolution of ZEKE and photodetachment microscopy; cryo-SEVI was developed to fill this niche.

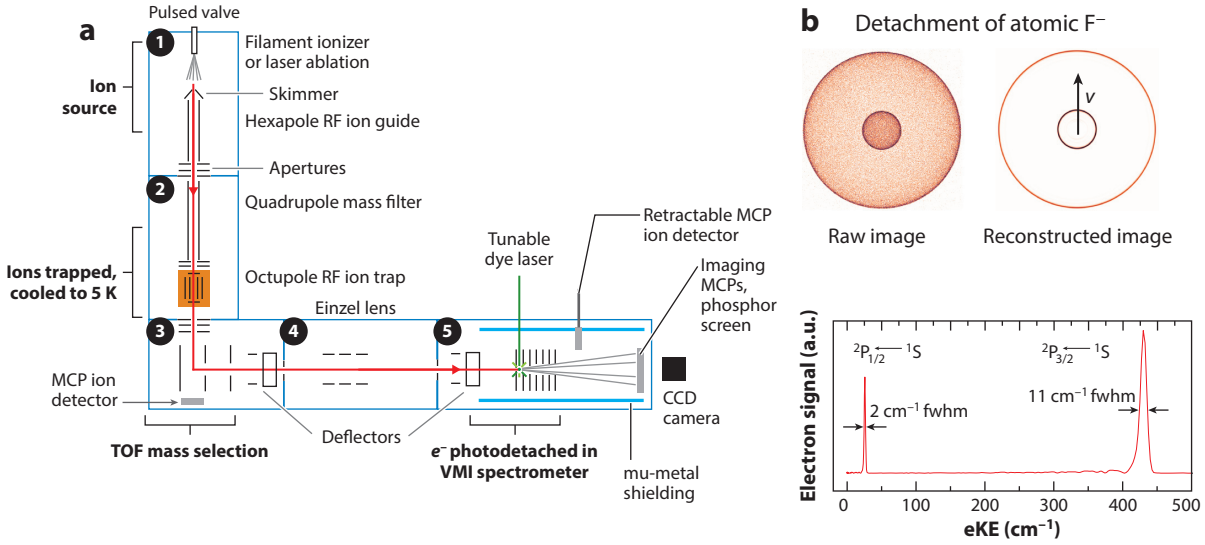

Figure 2

(*a*) Current configuration of the Berkeley cryo-SEVI apparatus. Ions are generated in a pulsed ion source, cryogenically cooled in a RF ion trap, mass-selected by TOF, and photodetached with a tunable laser at various fixed wavelengths. A VMI spectrometer (40) focuses the resulting photoelectrons onto an imaging detector (39). (*b*) Experimental raw and reconstructed images from detachment of atomic F^- at 358.9 nm, and the photoelectron spectrum in kinetic energy space after radial integration of the reconstructed image and conversion from velocity space to kinetic energy space. Abbreviations: CCD, charge-coupled device; cryo-SEVI, slow photoelectron velocity-map imaging of cryogenically cooled anions; eKE, electron kinetic energy; fwhm, full width at half-maximum; MCP, microchannel plate; RF, radiofrequency; TOF, time of flight; VMI, velocity-map imaging.

3. ANION CRYO-SEVI

Cryo-SEVI is a high-resolution variant of earlier pulsed photoelectron imaging experiments. The current version of the Berkeley cryo-SEVI apparatus is shown in **Figure 2*a*** and has been described in detail elsewhere (32–34).

Three experimental conditions allow for improved energy resolution:

- Low VMI extraction voltages magnify the photoelectron image on the position-sensitive detector, selectively detecting the slowest electrons and leading to better-resolved features. The VMI lens is also mounted collinearly with the ion flight path, eliminating contributions of ion velocity spread to the photoelectron energy resolution.
- Photodetachment is carried out close to threshold for each transition of interest, yielding low-eKE photoelectrons. Because VMI spectrometers have a relatively constant ΔeKE/eKE (40), the absolute energy resolution is best for small eKE, as shown in **Figure 2*b***. New VMI lens designs have also demonstrated significantly improved ΔeKE/eKE (61–64).
- Ions are trapped in a cryogenically cooled radio-frequency ion trap held at $T = 5$ K (65, 66), where they are thermalized to their ground vibrational and electronic states through collisions with buffer gas (67) in order to limit spectral congestion by eliminating hot bands, sequence bands, and rotational broadening (34).

Under these conditions, SEVI can achieve energy resolution of ∼1 cm^{-1} full width at half-maximum (fwhm) for atomic systems and molecular peak widths down to 2–3 cm^{-1} fwhm (62, 64, 68). The energy resolution is best for slow electrons, so a SEVI spectrum is typically obtained by

tuning the photodetachment laser wavelength through a particular photodetachment band in steps of 50–500 cm^{-1}. The high-resolution spectra obtained over each energy window are then stitched together and appropriately normalized (see Section 4.1) to create a composite high-resolution SEVI trace.

Several research groups have developed similar photoelectron imaging experimental capabilities. Wang and coworkers (69, 70) use a high-resolution VMI spectrometer coupled to an electrospray ionization (ESI) ion source and a cryogenic ion trap, while von Issendorff and coworkers (71) have coupled a cryogenic trap to a conventional photoelectron imaging setup. Ning and coworkers developed a high-resolution imaging spectrometer (68) and have recently added cryo-cooling capabilities (72). The Heaven group (73) has recently reported results from a new SEVI setup, and a new cryo-SEVI instrument is also in development in the Garand group (74). The Lineberger group (75, 76) uses a VMI photoelectron spectrometer that can be operated in a SEVI mode. Work to develop new photoelectron imaging capabilities is also ongoing in the Sanov (77) and Gibson (78) laboratories.

4. APPLICATIONS

4.1. Vibrational Structure of Polycyclic Aromatic Hydrocarbon Radicals

The spectroscopy of free radicals has been a frontier area for many years because of their reactive nature and spectroscopic complexity (79, 80). Anion PES is a powerful and versatile method for investigating free radicals, which almost always have positive EAs. The corresponding anions are often closed-shell species that are straightforward to generate, after which they are mass-selected and photodetached to form the radical of interest. The resulting photoelectron spectrum maps out the energetics and vibronic structure of the free radical (15).

These capabilities are enhanced with the ion cooling and high resolution afforded by cryo-SEVI, as demonstrated in work where we extract accurate EAs, fundamental vibrational frequencies, and term energies of low-lying electronic states of organic radicals (81, 82) for which conventional anion PES yielded largely unresolved spectra (83). Our recent study of the 9-, 1-, and 2-anthracenyl ($C_{14}H_9$) radicals exemplifies the capabilities of cryo-SEVI to investigate specific radical isomers with many low-frequency vibrational modes and congested FC envelopes (64). As polycyclic aromatic hydrocarbon radicals, these species are important combustion intermediates (84) and may be carriers of anomalous infrared (IR) emission bands in the interstellar medium (85).

The structures of the three anthracenyl anion isomers are shown in **Figure 3**. Specific anthracenyl isomers are prepared by reacting 9-, 1-, and 2-trimethylsilyl-anthracene precursors with F^-, which selectively forms the respective deprotonated 9-, 1-, or 2-anthracenyl anion thanks to the strong fluorine–silicon bond (86). This gas-phase synthesis has also been used to prepare specific anion isomers in SEVI studies of the propynyl, naphthyl, and furanyl radicals (82, 87, 88).

Cryo-SEVI spectra of the 9-, 1-, and 2-anthracenyl electronic ground states are shown in **Figure 3**. First, a low-resolution overview spectrum is measured at a photon energy well above the eBE of the band of interest. Each peak in the composite high-resolution spectrum is scaled to match the intensity of the overview spectrum to minimize threshold effects that can distort relative peak intensities. Density functional theory (DFT) FC simulations are also plotted. The spectra of all three isomers show dense but well-resolved vibrational structure that is accurately predicted by FC simulation.

Considerable vibronic and structural information can be extracted from cryo-SEVI spectra. In each panel of **Figure 3**, the peak at lowest eBE represents the vibrational origin (0_0^0 transition),

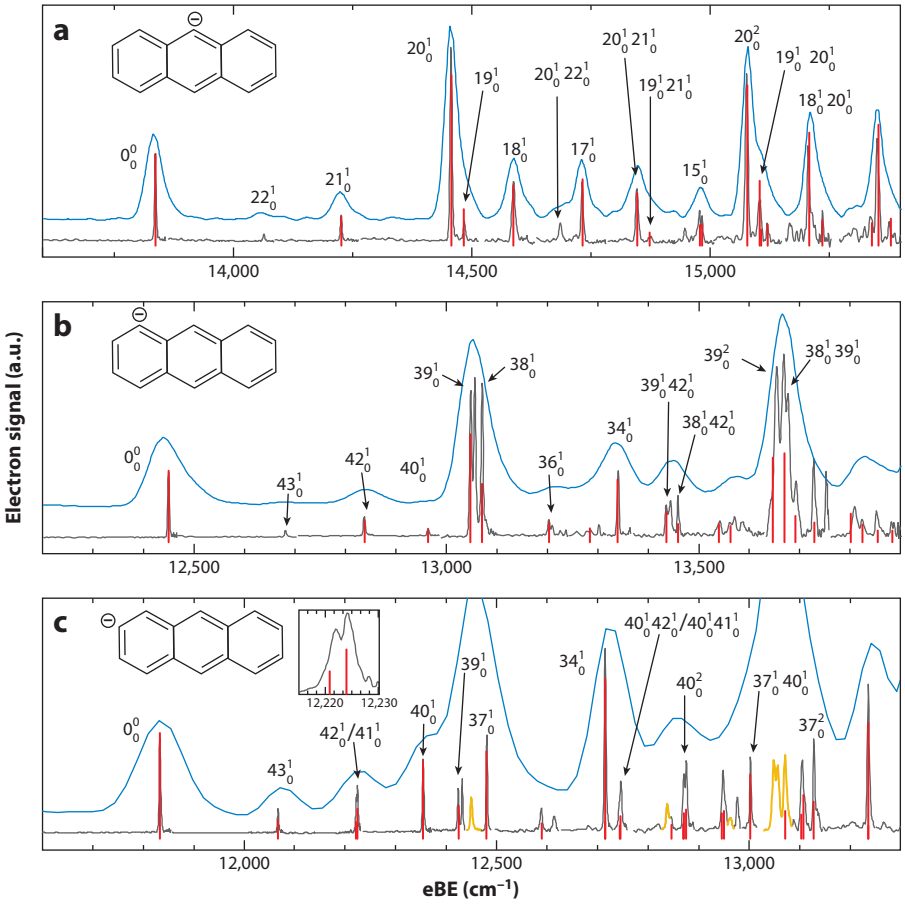

Figure 3

SEVI spectra of photodetachment to (*a*) the $\tilde{X}^2A_1$ ground state of 9-anthracenyl and the $\tilde{X}^2A'$ ground states of (*b*) 1-anthracenyl and (*c*) 2-anthracenyl. Low-resolution overview scans are shown in blue and high-resolution traces in dark gray. Peaks indicating some contamination of the 1-anthracenyl isomer in the 2-anthracenyl spectrum are plotted in yellow in panel *c*. DFT FC simulations are shown in red. Abbreviations: DFT, density functional theory; eBE, electron binding energy; FC, Franck–Condon; SEVI, slow photoelectron velocity-map imaging. Figure adapted from Reference 64 with permission.

yielding experimental EAs of 1.7155 eV, 1.5436 eV, and 1.4671 eV for the 9-, 1-, and 2-anthracenyl radicals. The decrease in EA as the site of deprotonation is moved from C_9 to C_1 to C_2 reflects the energetic ordering of the anions. DFT calculations find that the 9-anthracenyl anion is lowest-lying, while the 1-anthracenyl and 2-anthracenyl anions lie 0.13 eV and 0.18 eV higher in energy. By contrast, the 9-, 1-, and 2-anthracenyl radicals are nearly isoenergetic, falling within 0.02 eV of one another.

The cryo-SEVI spectra show extensive vibrational structure, which can be attributed nearly entirely to fundamentals, progressions, and combination bands of totally symmetric FC-active modes in the anthracenyl radicals. The ion temperature and instrumental resolution are sufficient to distinguish the 2-anthracenyl ν_{41} and ν_{42} fundamentals (inset of **Figure 3*c***), which are split by less than 3 cm^{-1}. The most highly FC-active modes for each radical involve significant motion near

the deprotonated site, as photodetachment removes an electron from an *s-p* hybridized molecular orbital localized at that site. This is also consistent with DFT calculations, which suggest that the C–C–C interior bond angle at the deprotonated site widens by ∼14° in all three systems upon detachment to the radical ground state.

Dipole-bound state (DBS): a weakly bound state where an electron is bound by interaction with the molecular dipole moment

4.2. Conformation-Specific Cryo-SEVI via Resonant Autodetachment

SEVI spectra can be complicated by resonantly enhanced phenomena mediated by metastable anion excited states. If an anion excited state lies within the manifold of neutral states, excitation to vibrational levels of this state can compete with direct detachment to the neutral. The anion excited state can then undergo autodetachment by converting vibrational, rotational, or electronic energy into the electronic energy required to detach an electron (31, 89). The overall process is given by

$$A^- + h\nu \rightarrow A^{-*} \rightarrow A + e^-. \qquad 3.$$

The distribution of neutral states formed by autodetachment generally differs from direct detachment, resulting in a photoelectron spectrum that is not governed by FC factors. For example, vibrational autodetachment often occurs according to a vibrational propensity rule that favors the loss of one vibrational quantum (31).

Autodetachment has two distinct experimental signatures. It can result in a structured total photodetachment cross section, in contrast to the smoothly varying cross sections associated with direct detachment (Equation 1). Its signature in a photoelectron spectroscopy experiment is the appearance of new vibrational features or significant change in relative intensities of existing features as a function of photodetachment energy, as one passes in and out of resonance with the autodetaching state.

As an example of the complex interplay between direct detachment and autodetachment, Wang and coworkers (90) have perfected a spectroscopic technique that combines cryo-SEVI with mode-specific vibrational autodetachment from a diffuse dipole-bound state (DBS) of the anion of interest. By acquiring cryo-SEVI spectra at specific, resonant photon energies, this method can illuminate both the FC-forbidden vibrational structure of the neutral and the autodetaching vibrational levels of the DBS. The high resolution and spectral clarity afforded by cryo-SEVI is necessary to resolve the specific neutral features populated by autodetachment. A number of radical species have been probed with this method, including phenoxy (90); 2-hydroxyphenoxy (91); and deprotonated uracil (92, 93), thymine (94), and 2-hydroxypyrimidine (95).

Because the resonant autodetachment process is state-selective, it can be used to distinguish the spectroscopic contributions from different conformers. The DBS of a single conformer can be resonantly excited; it then autodetaches to populate the neutral vibrational levels of that conformer, enhancing the SEVI signal of one species over the other. While separation of two conformers connected by a hindered rotation is impossible at temperatures where the barrier is energetically accessible, the low temperatures achieved in a cryogenic ion trap freeze out static populations, which can then be probed independently.

The Wang group (70, 96) has used this technique to disentangle cryo-SEVI spectra of the two 3-hydroxyphenoxy (3-HPO) radical conformers. The two 3-HPO conformers are shown in **Figure 4*a***. Both *syn* and *anti* 3-HPO have sufficient dipole moments to support a DBS, whose binding energies can be measured via threshold photodetachment (96). The anions are prepared in an ESI source and cooled in a cryogenic trap. While the *syn* conformer is calculated to be slightly more stable than the *anti* conformer, they are close enough in energy that both species are formed and observed experimentally. The nonresonant SEVI traces shown in **Figure 4*b*** show

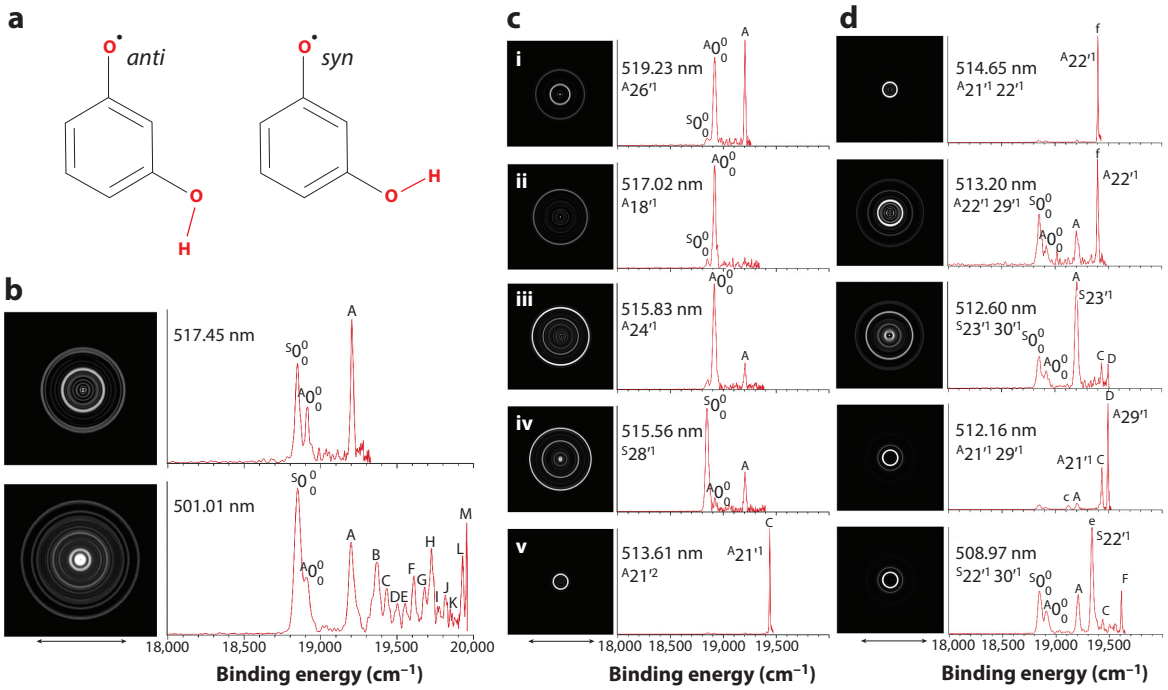

Figure 4

(*a*) Schematic structures of the *anti* and *syn* *m*-HO(C_6H_4O) conformers. Representative (*b*) nonresonant and (*c*,*d*) resonant cryo-SEVI images and spectra of *m*-HO(C_6H_4O)$^-$ taken at various detachment wavelengths. Peaks labeled with A and S superscripts represent vibrational levels of the *anti* and *syn* conformers, respectively. Abbreviation: cryo-SEVI, slow photoelectron velocity-map imaging of cryogenically cooled anions. Figure adapted from Reference 70 with permission of AIP Publishing.

contributions from both *syn* and *anti* 3-HPO, with the vibrational origins of the two species split by 67 cm^{-1}.

The cryo-SEVI spectra show features and relative intensities that vary strongly with wavelength, indicating contributions from resonant autodetachment; representative traces are shown in **Figure 4*c*,*d***. The resonantly accessed DBS states and the neutral levels populated after autodetachment can be assigned through comparison with calculated DFT frequencies and measured DBS binding energies of the two conformers.

Figure 4*c*(*i*–*iv*) shows cryo-SEVI traces taken at photon energies that resonantly excite vibrational fundamentals of either the *syn* or *anti* DBS, which then autodetach by loss of a single vibrational quantum to populate the corresponding *syn* or *anti* vibrational origin. The SEVI traces in **Figure 4*c*(*v*),*d*** result from resonant excitations of combination band and overtone DBS states, which autodetach to preferentially populate relevant neutral vibrational fundamentals. In total, Wang and coworkers mapped out more than 30 DBS resonances of *syn* and *anti* 3-HPO, which aided in the characterization of 14 vibrational fundamentals of the two conformers, including several FC-forbidden modes inaccessible with conventional cryo-SEVI.

4.3. Structural Isomers of Metal Oxide Clusters

Catalysts based on transition metal oxides catalyze many fundamental chemical reactions. Hence, there is considerable interest in developing a molecular-level understanding of what underlies

this chemistry. Many of the reactive properties of surfaces arise from defect sites, where the local stoichiometry and bonding motifs differ from the bulk crystal structure; uncovering the detailed reaction mechanisms at these active sites is a fundamental goal of physical chemistry (97). These considerations have motivated studies of gas-phase metal oxide clusters that, in addition to being tractable for both experimental and computational study, have a high proportion of reactive surface atoms analogous to bulk surface defects (98). Clusters display dramatically different structures and reactivity as a function of size; their study can therefore elucidate the evolution of properties and emergence of macroscopic phenomena as one moves toward the bulk. By determining how the size and composition of a cluster govern its reactivity, one can gain insight into the workings of bulk catalysts (99, 100).

The spectroscopy of transition metal oxide clusters can be challenging, and contributions from multiple low-lying spin states (101, 102), electronic configurations (103, 104), and structural isomers (105, 106) must be considered. The study of these species with anion PES has been limited by poor vibrational resolution resulting from numerous low-frequency vibrational modes and warm ion temperatures, as clusters formed in a laser ablation source heat up during condensation (107, 108). The development of cryo-SEVI has made tractable the full vibrational characterization of size-selected metal oxide clusters, even those composed of multiple transition metal atoms (101, 102). As an example, our study of the $Ti_2O_4^-$ and $Zr_2O_4^-$ anions (109) allowed for conclusive determination of the minimum-energy and next lowest-lying structures of these species and served as a confirmation of high-level theoretical work.

The $M_2O_4^{-/0}$ (M = Ti, Zr) clusters have three possible low-energy geometries, as shown in **Figure 5*a***. Anion photoelectron spectra have been reported in the literature for $Ti_2O_4^-$, but

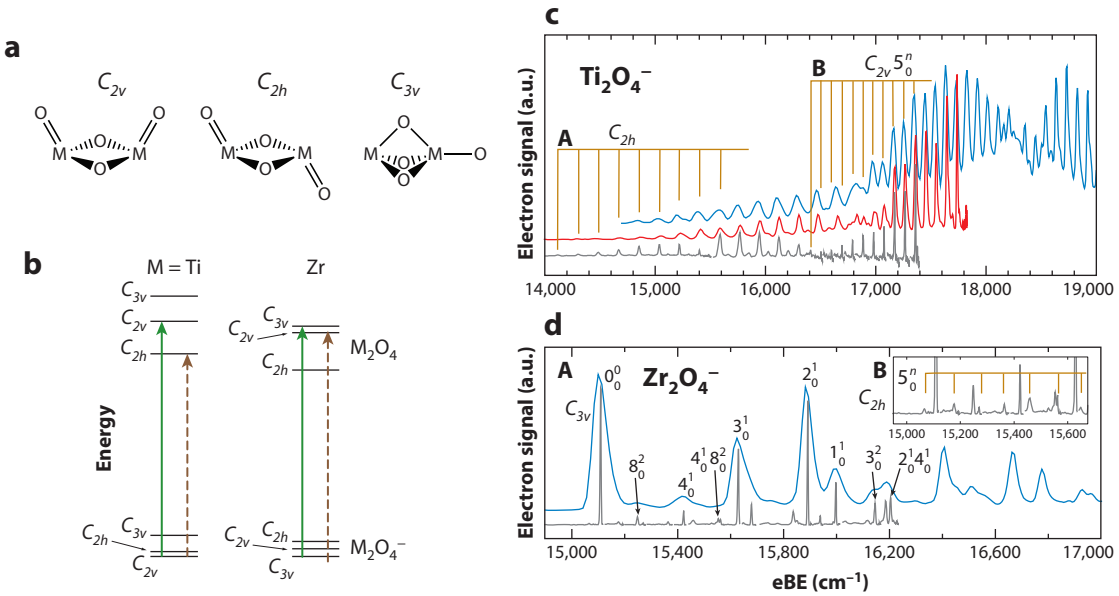

Figure 5

(*a*) Schematic structures for the three relevant M_2O_4 (M = Ti, Zr) structural isomers and (*b*) energy level diagram of the isomers and charge states of Ti_2O_4 and Zr_2O_4. Cryo-SEVI spectra of (*c*) $Ti_2O_4^-$ and (*d*) $Zr_2O_4^-$ showing overview traces in blue and red and composite high-resolution traces in gray. Abbreviations: cryo-SEVI, slow photoelectron velocity-map imaging of cryogenically cooled anions; eBE, electron binding energy. The energies in panel *b* are from CCSD(T) calculations by Li & Dixon (111, 112). Figure adapted from Reference 109 with permission.

with insufficient energy resolution to resolve any vibrational structure, making assignment of a structural isomer unclear (23, 110). Li & Dixon (111, 112) carried out CCSD(T) calculations for the $M_2O_4^{-/0}$ (M = Ti, Zr) species and found that the $Ti_2O_4^-$ and $Zr_2O_4^-$ anions take on C_{2v} and C_{3v} geometries, respectively, although the other structures are low-lying (**Figure 5*b***). These calculations indicated that, while the $M_2O_4^-$ structures should have similar EAs, resolution of vibrational structure and comparison to FC simulation would allow for distinction between isomers.

The cryo-SEVI spectra of $Ti_2O_4^-$ and $Zr_2O_4^-$ are shown in **Figure 5*c*,*d***. The $Ti_2O_4^-$ spectrum shows a weak but extended progression of peaks spaced by ~180 cm^{-1} (band A), which becomes buried under more intense photoelectron signal at higher eBE with a peak spacing of 95 cm^{-1} (band B). The $Zr_2O_4^-$ spectrum also shows two overlapping bands, one considerably more intense than the other, with differing characteristic peak spacings: Band A begins with a strong vibrational origin and has irregularly spaced vibrational structure, while band B underlies it with a weak progression of peaks spaced by 95 cm^{-1}. For both $M_2O_4^-$ species, bands A and B have distinct anisotropies in the SEVI images, suggesting that they correspond to two different photodetachment transitions.

The two bands are assigned to photodetachment of distinct anion isomers, each landing in a neutral state with the same corresponding molecular structure. The contribution of different anion isomers can be assigned by comparison to FC simulations; when vibrational features are fully resolved, the different isomers have strikingly different spectral fingerprints. For $Ti_2O_4^-$, the 180-cm^{-1} and 95-cm^{-1} spacings of band A and band B match well, respectively, with the calculated FC-active terminal oxygen wagging modes of the neutral C_{2h} and C_{2v} isomers. In $Zr_2O_4^-$, the strong vibrational origin and several FC-active modes of band A match the predicted photoelectron spectrum of the C_{3v} isomer. The 95-cm^{-1} spacing of the $Zr_2O_4^-$ band B, like that of the $Ti_2O_4^-$ spectrum, clearly points to the C_{2v} isomer.

Our preparation of cold ions is likely to favor the most stable anion isomers. Considering the most intense band in the spectrum of each $M_2O_4^-$ species, it appears that the lowest-energy anion isomers are the C_{2v} structure for $Ti_2O_4^-$ and the C_{3v} structure for $Zr_2O_4^-$. Based on the assignment of the weaker bands, the second-lowest-energy isomers are the C_{2h} and C_{2v} structures for $Ti_2O_4^-$ and $Zr_2O_4^-$, respectively. The observed ordering agrees with the calculations of Li & Dixon (**Figure 5*b***). Even the relatively simple $M_2O_4^-$ clusters have proved challenging to model computationally, and the cryo-SEVI results provide an important experimental benchmark to confirm the structures, frequencies, and energetics of these species. The natural extension of this work is to study the reactive complexes of metal oxide clusters with small molecule substrates as more explicit models for catalysis, in line with the work of Jarrold and coworkers (113).

4.4. Structures and Low-Frequency Vibrations of Noble Metal Clusters

Despite the fact that bulk gold is quite inert, gold nanostructures have high catalytic activity and varied applications in materials science, sensing, and electronics (114). As with the metal oxide clusters discussed in Section 4.3, the study of gas-phase gold clusters is a good starting point to gain insight into their size-dependent geometries, electronic structure, and behavior (115). Noble metal clusters can also be doped with atoms of other elements to form alloys with new and tunable properties.

Wang and coworkers (116, 117) have carried out several anion PES studies of pure and doped gold clusters. With their high-resolution SEVI work on the Au_4^- (118) and $Au_2Al_2^-$ (119) clusters, they have been able to confirm the geometries of these species and resolve very low-frequency vibrational structure. Clusters were formed by laser ablation of either a pure gold or mixed gold-aluminum target, with helium carrier gas seeded with argon. While the Wang

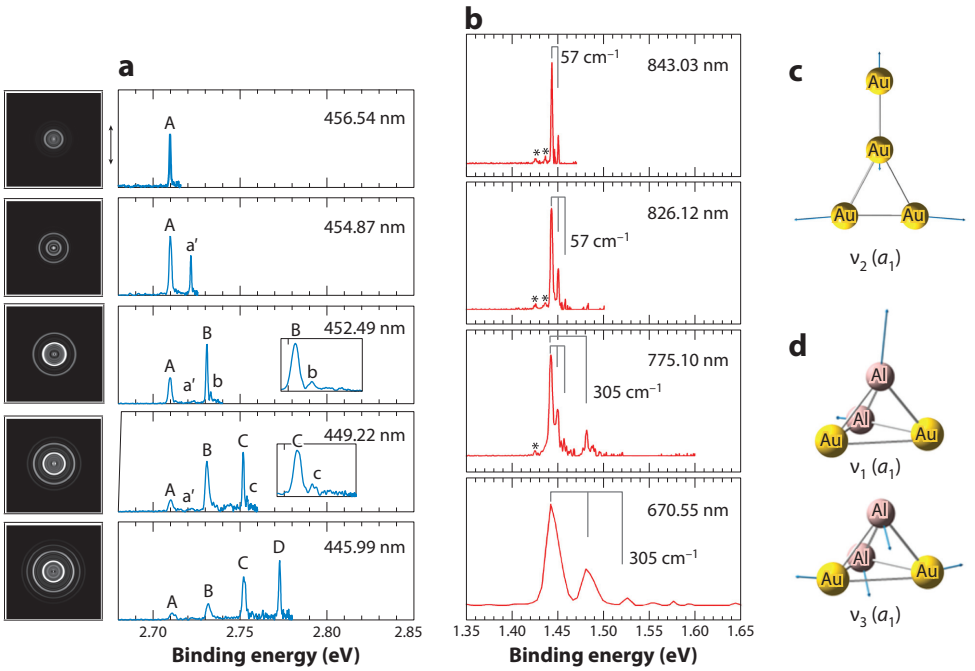

Figure 6

(*a*) Photoelectron images and spectra of Au_4^- and (*b*) spectra of $Au_2Al_2^-$ at various detachment wavelengths, and geometrical structures and FC-active vibrational mode displacements for (*c*) Au_4^- and (*d*) $Au_2Al_2^-$. Panels *a* and *c* adapted from Reference 118 with permission. Panels *b* and *d* adapted from Reference 119 with permission.

group does not have a cryogenic ion trap coupled to their laser ablation source, the clusters appear to be produced under sufficiently cold conditions for spectroscopic clarity.

Earlier PES studies of Au_4^- reveal only partial vibrational structure for this species (120, 121), but ion mobility measurements (122) and theory (123) suggest that the ground-state anion isomer has a planar C_{2v} Y-shaped structure, as shown in **Figure 6*c***. While neutral Au_4 is predicted to take on a planar D_{2h} rhombus structure (123), vertical detachment from the anion ground state will yield information about the C_{2v} neutral isomer.

The SEVI spectra shown in **Figure 6*a*** confirm the assignment of Au_4^- to the C_{2v} isomer. The spectra are dominated by a vibrational progression (peaks A, B, C, etc.) with a fundamental frequency of 171 cm^{-1}. Spectra taken under warm source conditions show that a hot band appears below the vibrational origin, yielding the corresponding frequency of 135 cm^{-1} for Au_4^-. These frequencies are assigned to the ν_2 vibrational mode, whose displacement is shown in **Figure 6*c***. Mode ν_2 is expected to be highly FC active, as it corresponds to significant Au–Au stretching in the base of the Au_3 moiety, and detachment of Au_4^- removes an electron from an antibonding molecular orbital localized to these two atoms. The localization of this orbital also leads to an increase of 40 cm^{-1} in the calculated ν_2 frequency from anion to neutral, in good agreement with what is observed experimentally.

The $Au_2Al_2^{-/0}$ alloy clusters, interestingly, both prefer C_{2v} tetrahedral geometries, with little geometry change upon detachment. The SEVI traces of $Au_2Al_2^-$ shown in **Figure 6*b*** reveal two short vibrational progressions with frequencies of 305 cm^{-1} and 57 cm^{-1}. These correspond to

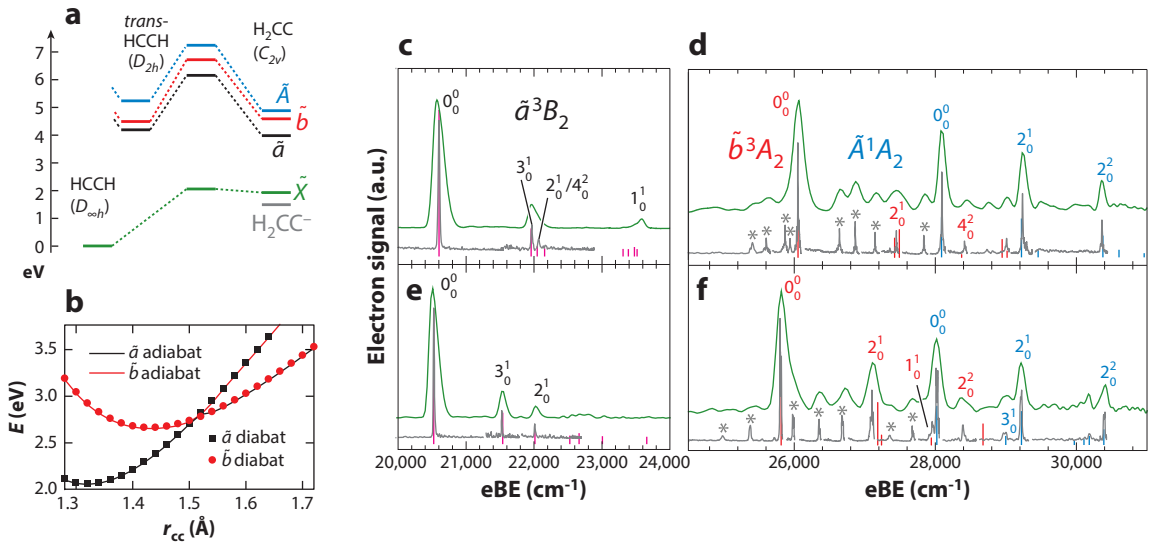

Figure 7

(*a*) Energy level diagram for the low-lying electronic states of the vinylidene-acetylene system as well as the corresponding anions. (*b*) One-dimensional potential curves of the adiabatic and diabatic vinylidene states, showing the conical intersection between the $\tilde{a}$ and $\tilde{b}$ triplet states near the $\tilde{b}$ state minimum. Also shown are cryo-SEVI spectra of (*c*,*d*) H_2CC^- and (*e*,*f*) D_2CC^-, showing detachment to the (*c*,*e*) $\tilde{a}^3B_2$ and (*d*,*f*) $\tilde{b}^3A_2$ and $\tilde{A}^3A_2$ electronic excited states. Green and gray curves are overview and high-resolution composite spectra, respectively. Calculated stick spectra are also shown for the $\tilde{a}^3B_2$ (*dark pink*), $\tilde{b}^3A_2$ (*red*), and $\tilde{A}^3A_2$ (*blue*) states. Asterisks indicate irregular spectral structure arising from strong coupling between the $\tilde{a}$ and $\tilde{b}$ states near the conical intersection. Abbreviations: cryo-SEVI, slow photoelectron velocity-map imaging of cryogenically cooled anions; eBE, electron binding energy. Figure adapted from Reference 129 with permission. Copyright 2016 American Chemical Society.

modes ν_1 and ν_2 (**Figure 6*d***). Two hot bands, labeled with asterisks, lie below the vibrational origin and report on the two lowest-frequency totally symmetric modes of the anion.

It is compelling that the $Au_2Al_2^{-/0}$ alloy clusters take on a three-dimensional tetrahedral geometry, while the pure $Au_4^{-/0}$ clusters prefer planar geometries, albeit two different ones. Pure gold clusters are thought to prefer planar structures because of relativistic effects that enhance *5d-6s* hybridization and lead to very directional bonding (124). The SEVI results indicate that this preference is disrupted by interactions with aluminum atoms, suggesting that the nanoscale geometries of these species are highly tunable as a function of composition.

4.5. Nonadiabatic Vibronic Structure of Vinylidene

Vinylidene (H_2CC), the simplest unsaturated carbene, is a high-energy isomer of acetylene with a very low barrier to isomerization in its ground singlet electronic state (**Figure 7*a***). As a result, neutral vinylidene is difficult to isolate, and much spectroscopic work has instead searched the high-lying states of acetylene for traces of isomerization and mixing with the vinylidene well (125). Anion PES provides a more direct method to probe this species, as H_2CC^- constitutes the global minimum isomer on the anionic $C_2H_2^-$ surface. H_2CC^- is easily synthesized in the gas phase by deprotonating ethylene (C_2H_4) with O^-; its vibrational spectrum has been characterized using infrared two-photon photodetachment and one-photon autodetachment (126). Detachment from the H_2CC^- $\tilde{X}^2B_1$ state allows transitions to both singlet and triplet neutral states, as illustrated in **Figure 7*a***; previous anion PES experiments by Ervin et al. (127) illuminated the energetics and

some vibrational features of the H_2CC ground singlet state ($\tilde{X}\,^1A_1$) and low-lying $\tilde{a}$ and $\tilde{b}$ triplet states. In that work, features in the singlet band were observed to be considerably broader than in the triplet bands. Since the triplet states are predicted to have much higher isomerization barriers than the $\tilde{X}\,^1A_1$ state (128), this result was interpreted as an indication of rapid isomerization dynamics in the ground singlet state.

A recent cryo-SEVI study of the two lowest triplet ($\tilde{a}^3B_2$ and $\tilde{b}^3A_2$) and first excited singlet ($\tilde{A}^1A_2$) states of vinylidene provides a more complete picture of the complex vibronic structure of the excited electronic states of this species (129). Cryo-SEVI spectra of the $\tilde{a}$, $\tilde{b}$, and $\tilde{A}$ bands are shown in **Figure 7*c*,*d*** for H_2CC and **Figure 7*e*,*f*** for D_2CC, accompanied by high-level photodetachment simulations plotted as stick spectra. Calculations indicate that the energy ordering of these states is $\tilde{a} < \tilde{b} < \tilde{A}$ and that these three excited state surfaces demonstrate significant (~2 eV) barriers to isomerization to acetylene (**Figure 7*a***).

The $\tilde{a}^3B_2$ bands (**Figure 7*c*,*e***) exhibit regular vibrational structure assigned to totally symmetric vibrational states with reference to theoretical stick spectra in dark pink and prior work (not shown; see 127). At higher eBE, the overlapping $\tilde{b}^3A_2$ and $\tilde{A}^1A_2$ bands (**Figure 7*d*,*f***) are less straightforward to interpret. Comparison with the simulated stick spectra in blue allows identification of features arising from the $\tilde{A}$ band, which had been previously predicted (130) but not experimentally observed. The $\tilde{b}$ band vibrational origin has been reported before (127), but we newly resolve a collection of weak and irregular features (marked with asterisks) falling to either side, not reproduced by the simulated stick spectra in red.

The intensities of these irregular features are independent of ion temperature, indicating that they are not hot bands and instead reflect the vibronic structure of neutral H_2CC. The spacing of these features is too narrow to represent any harmonic frequencies of the $\tilde{b}$ state. The high isomerization barriers indicate that these irregular features do not reflect coupling to the acetylene well. Instead, it appears that these features result from nonadiabatic coupling with the nearby $\tilde{a}$ state. We identify a conical intersection (CI) between the $\tilde{a}$ and $\tilde{b}$ states lying only 0.05 eV above the $\tilde{b}$ state minimum (**Figure 7*b***). Near the CI, dark $\tilde{a}$ state vibrational levels can borrow intensity from close-lying bright FC-active levels of the $\tilde{b}$ state, as well as perturb their expected positions and intensities.

The vinylidene excited states clearly exhibit interesting vibronic behavior even in the absence of coupling into the acetylene well. In additional recent work (131), we discuss subtle effects of isomerization in the cryo-SEVI spectra of the vinylidene $\tilde{X}\,^1A_1$ ground state.

4.6. Transition State Spectroscopy of Bimolecular Reactions

Direct observation of the reaction transition state is one of the holy grails of chemistry (132). Characterization of this unstable species—its geometry, energy relative to the product and reactant asymptotes, and vibrational frequencies—can provide a wealth of information about the reactive potential energy surface and how it governs chemical behavior. Photodetachment of a bound anion similar in geometry to a neutral unimolecular or bimolecular transition state can yield a spectrum showing structure characteristic of the neutral potential energy surface (25, 26). It is possible to observe FC structure in modes perpendicular to the reaction coordinate and, more interestingly, sharper features corresponding to discrete quantum states that are quasibound along the reaction coordinate (26). Such resonances along the reaction coordinate can be very sensitive probes of the transition state region and are an exceptional point of comparison between theory and experiment.

The capabilities of cryo-SEVI transition state spectroscopy are well illustrated via the $F + H_2 \rightarrow H + HF$ reaction, a benchmark system for molecular beam scattering experiments

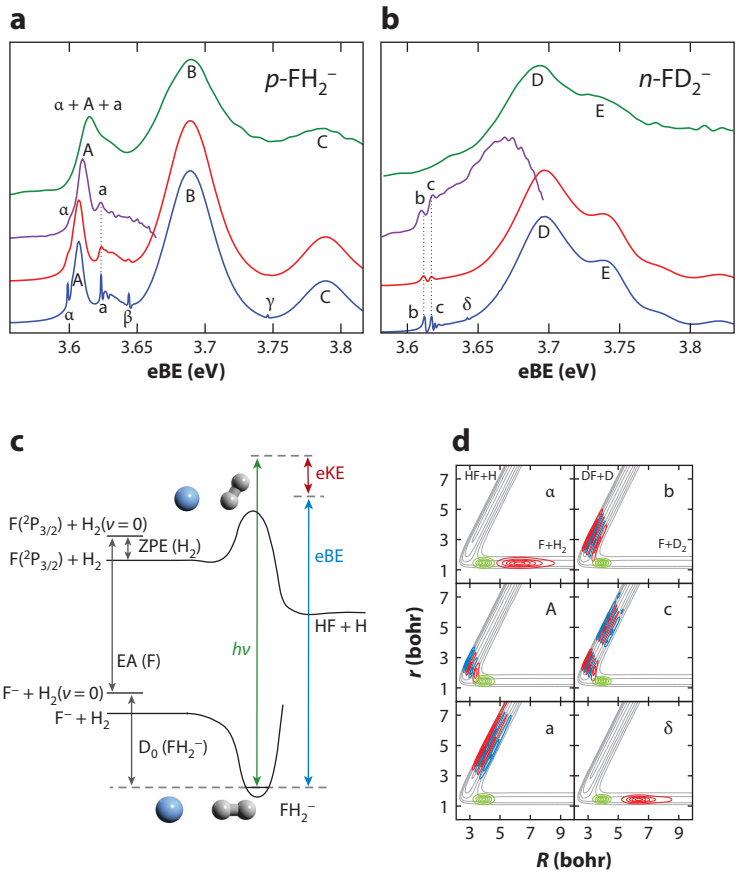

Figure 8

Photodetachment spectra of (*a*) *p*-FH_2^- and (*b*) *n*-FD_2^- showing experimental survey scans (*green*), high-resolution experimental scans (*purple*), and theoretical simulations at 1-meV (*blue*) and 3-meV (*red*) resolution. (*c*) Energy schematic of the FH_2^- photodetachment process and (*d*) wavefunctions of resonances. The wavefunctions are shown at the energies of the labeled peaks in panels *a* and *b* and are plotted in collinear geometry as red and blue contours, as a function of the distance *R* between F and the center of mass of H_2 (D_2) and the bond length *r* of H_2 (D_2). Superimposed in gray are contours of the potential energy surface of Lique et al. (140). Contours of the corresponding anion wave functions are shown in green. Abbreviations: EA, electron affinity; eBE, electron binding energy; eKE, electron kinetic energy; ZPE, zero-point energy. Figure adapted from Reference 139 with permission.

(133–135). The weakly bound FH_2^- anion has similar bond lengths to the neutral transition state, but is linear while the F + H_2 transition state is bent. The photoelectron spectrum is therefore dominated by a FC progression in the F–H–H bending motion. An energy diagram of this photodetachment process is shown in **Figure 8*c***. Early anion PES studies resolved the bending progression but saw no hints of sharper structure from reactive resonances (136). Calculations predicted that resonances should be observable with higher resolution (137), but their identification proved elusive in a preliminary SEVI study (138).

Revisiting the F + H_2 (D_2) reaction with cryo-SEVI finally allowed the resolution of resonances in the product and reactant wells and near the transition state (139). The FH_2^- (FD_2^-) anions

are produced by clustering F^- with H_2 (D_2) buffer gas at cryogenic temperatures in the ion trap, yielding considerably better ion signal than was achievable in a gas jet expansion. This proved essential for achieving high signal-to-noise in the cryo-SEVI measurements.

Low- and high-resolution cryo-SEVI spectra of *p*-FH_2^- and FD_2^- are plotted in **Figure 8*a*,*b*** alongside theoretical spectra that use new high-quality potential energy surfaces (140). Calculated scattering wavefunctions at the energy of each peak are extracted to facilitate assignment of the observed structure. **Figure 8*d*** shows plots of the wavefunctions in red and blue corresponding to the labeled spectral peaks; the initial anion wavefunctions are shown in green.

In addition to the previously observed bending FC progression (peaks A, B, and C for FH_2^- and peaks D and E for FD_2^-), we now resolve and assign several resonance features, representing bound or quasibound states supported by the reaction potential energy surface. Features α, A, and a in FH_2^- and peaks b and c in FD_2^- all manifest clearly in the accompanying simulations. The nature of these resonances is revealed by their localization and nodal structure in the wavefunction plots in **Figure 8*d***. Peak A had previously been assigned to a delocalized direct scattering state, but we now see that it is in fact a resonance localized near the $F + H_2$ transition state, with three quanta of excitation in the H–F stretching mode. Peaks a, b, and c are quasibound resonances supported by the H. . .H–F (D. . .D–F) product van der Waals well, with different quanta in the H–F (D–F) and H–HF (D–DF) stretching modes, while α is a weakly bound state supported by the F. . .H_2 reactant well. The product resonance corresponding to peak a had been predicted by Russell & Manolopoulos (137) in 1996, but peaks b and c in the FD_2^- spectrum had not previously been predicted or observed.

The cryo-SEVI study of $F + H_2$ demonstrated that high-resolution transition state spectroscopy experiments can serve as benchmarks for state-of-the-art theoretical treatment of bimolecular reactive surfaces. This motivated the application of the technique to a system with considerably more degrees of freedom, the 7-atom $F + CH_3OH \rightarrow HF + CH_3O$ reaction (141). Like the $F + H_2$ reaction, $F + CH_3OH$ represents a favorable case for transition state spectroscopy, with a hydrogen-bonded CH_3OHF^- anion similar in geometry to the transition state for abstraction of the hydroxyl H atom, as shown in **Figure 9*a***.

Cryo-SEVI spectra of CH_3OHF^- and CH_3ODF^- are shown in **Figure 9*c*,*d***, accompanied by a high-level quantum dynamical simulation of the CH_3OHF^- photodetachment spectrum in **Figure 9*b***. The spectra are dominated by broad steps (labeled *a*–*e*), with an *a*–*b* spacing of ∼3,600 cm^{-1} for CH_3OHF^- detachment and ∼2,700 cm^{-1} for CH_3ODF^-. Previous photodetachment experiments (142, 143) also observed this stepped structure and assigned it to an H−F stretching progression of the CH_3O−HF product complex (PC). The location of the structure with respect to the product and reactant asymptotes confirms that the observed structure lies in the PC well.

With cryo-SEVI, we resolve fine structure spaced by ∼200 cm^{-1} superimposed on the broad steps and not previously resolved. The nature of this structure can be explained with reference to the vibrational adiabatic potentials (VAPs) shown in **Figure 9*a***, which correlate to free HF(v) + CH_3O products. The spectral steps *a*–*e* each represent detachment to an HF($v = 0$–4) VAP, while the fine peaks within each step are resonances supported in the PC VAP wells with excitation in the CH_3O−HF stretching mode. This assignment is confirmed with reference to the nodal structure of wavefunctions extracted from the quantum dynamical simulations (**Figure 9*e***). For instance, the *a1*, *b1*, and *c1* wavefunctions show an increasing number of nodes along the H−F stretching axis, while the *a1*, *a2*, and *a3* wavefunctions add nodes along the CH_3O−HF stretching axis.

While the states in feature *a* are bound with respect to the product asymptote, the states in features *b*–*e* are metastable and will eventually dissociate via vibrational predissociation as H–F stretching energy flows to translational motion along the reaction coordinate. As all resonances

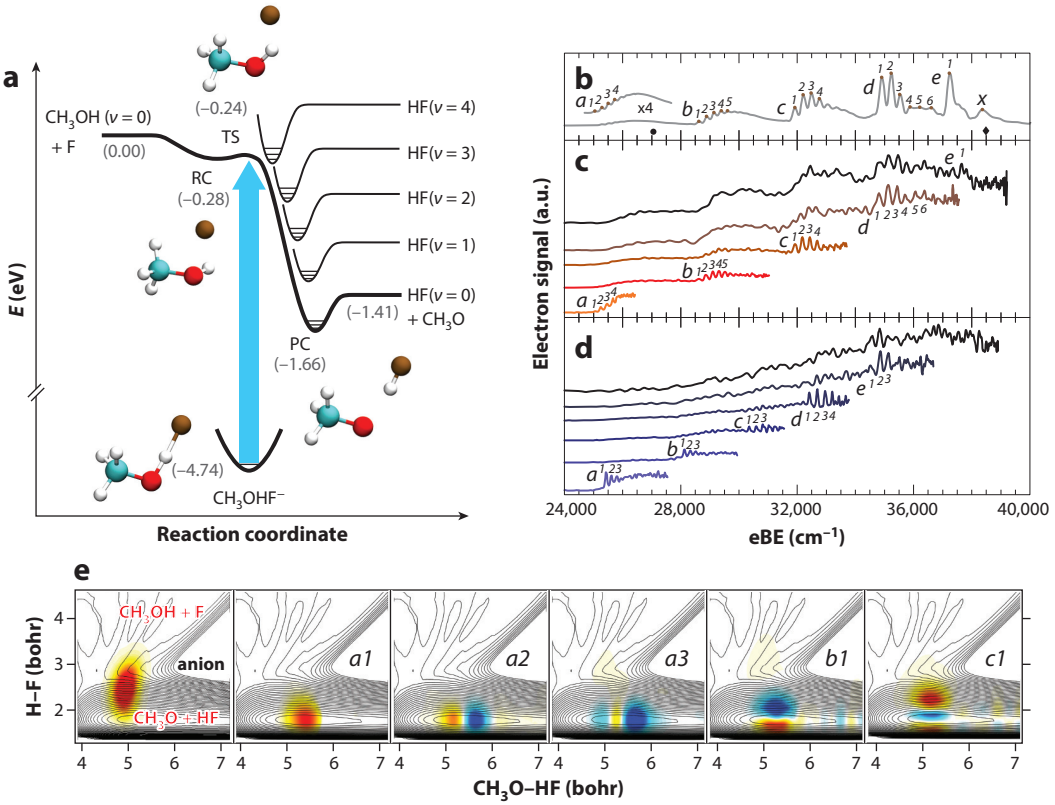

Figure 9

(*a*) Energy schematic for photodetachment of the CH_3OHF^- anion to the neutral $F + CH_3OH \rightarrow HF + CH_3O$ potential energy surface, showing geometries for the anion, reactant complex (RC), transition state (TS), nd product complex (PC) stationary points. (*b*) Theoretical simulation of the CH_3OHF^- photoelectron spectrum and experimental cryo-SEVI spectra of (*c*) CH_3OHF^- and (*d*) CH_3ODF^-. The • and ♦ symbols represent the product and reactant asymptotes, respectively. (*e*) Cuts of the CH_3OHF^- anion vibrational ground state wavefunction and representative $F + CH_3OH \rightarrow HF + CH_3O$ resonance wavefunctions. Other abbreviations: cryo-SEVI, slow photoelectron velocity-map imaging of cryogenically cooled anions; eBE, electron binding energy. Figure adapted from Reference 141 with permission.

seen here also lie below the reactant asymptote, they are inaccessible to reactive scattering experiments and therefore uniquely accessible with an anion PES scheme. Despite the complexity of the $F + CH_3OH$ system, this study shows that its key dynamical features can still be captured by a relatively simple physical picture.

5. SUMMARY AND OUTLOOK

Since our last review of the SEVI technique (33), new developments in cryogenic ion cooling and velocity-map imaging have allowed for photodetachment studies of a wide range of complex systems with excellent spectral clarity. The versatility of the cryo-SEVI technique in application to nearly any bound anion has allowed for high-resolution studies of free radicals, metal-containing clusters, nonadiabatic effects in the excited states of small molecules, and transition state spectroscopy of neutral reactive surfaces and metastable species. Recent cryo-SEVI work has shone

light on decades-old questions in benchmark systems such as the metastable vinylidene carbene and the $F + H_2$ reaction, and theoretical advances have aided significantly in the interpretation of these results.

Several promising future directions for the cryo-SEVI technique involve the incorporation of more diverse means to synthesize and isolate exotic anions. We have begun work with a new laser ablation cluster reactor source to study complexes of metal oxide clusters with small molecule substrates (144). Another interesting possibility is to couple an ion mobility drift tube to the cryo-SEVI spectrometer in order to separate different conformers (145). This could easily be coupled to an ESI anion source, which has already been used with cryo-SEVI by the Wang group (69) to great effect. Also of interest are more extensive tunable laser sources with which to probe these species. We have recently built a difference frequency generation laser setup to generate tunable IR light down to 4 μm (131) for high-resolution studies of species with low EAs.

The cryo-SEVI method has become established as a general and widely applicable spectroscopic tool, as is evidenced by its adoption in laboratories worldwide and its increasingly creative application to diverse molecular systems. Promising developments are to be expected for many years to come.

DISCLOSURE STATEMENT

The authors are not aware of any affiliations, memberships, funding, or financial holdings that might be perceived as affecting the objectivity of this review.

ACKNOWLEDGMENTS

The authors acknowledge support from the Air Force Office of Scientific Research under grant FA9550–16–1–0097 and from the Director, Office of Basic Energy Sciences, Chemical Sciences Division of the US Department of Energy under contract DE-AC02-05CH11231. M.L.W. thanks the National Science Foundation for a graduate research fellowship.

LITERATURE CITED

1. Zádor J, Taatjes CA, Fernandes RX. 2011. Kinetics of elementary reactions in low-temperature autoignition chemistry. *Prog. Energy Combust. Sci.* 37:371–421
2. Osborn DL. 2017. Reaction mechanisms on multiwell potential energy surfaces in combustion (and atmospheric) chemistry. *Annu. Rev. Phys. Chem.* 68:233–60
3. Seinfeld JH, Pandis SN. 1998. *From Air Pollution to Climate Change*. New York: Wiley
4. Seakins PW, Blitz MA. 2011. Developments in laboratory studies of gas-phase reactions for atmospheric chemistry with applications to isoprene oxidation and carbonyl chemistry. *Annu. Rev. Phys. Chem.* 62:351–73
5. Tielens AGGM. 2013. The molecular universe. *Rev. Mod. Phys.* 85:1021–81
6. Kaiser RI, Parker DSN, Mebel AM. 2015. Reaction dynamics in astrochemistry: low-temperature pathways to polycyclic aromatic hydrocarbons in the interstellar medium. *Annu. Rev. Phys. Chem.* 66:43–67
7. Castleman AW. 2011. Cluster structure and reactions: gaining insights into catalytic processes. *Catal. Lett.* 141:1243–53
8. Tyo EC, Vajda S. 2015. Catalysis by clusters with precise numbers of atoms. *Nat. Nanotechnol.* 10:577–88
9. Domcke W, Yarkony DR. 2012. Role of conical intersections in molecular spectroscopy and photoinduced chemical dynamics. *Annu. Rev. Phys. Chem.* 63:325–52
10. Guo H, Yarkony DR. 2016. Accurate nonadiabatic dynamics. *Phys. Chem. Chem. Phys.* 18:26335–52
11. Levine RD. 2005. *Molecular Reaction Dynamics*. Cambridge: Cambridge Univ. Press

12. Guo H, Liu K. 2016. Control of chemical reactivity by transition-state and beyond. *Chem. Sci.* 7:3992–4003
13. Rienstra-Kiracofe JC, Tschumper GS, Schaefer HF, Nandi S, Ellison GB. 2002. Atomic and molecular electron affinities: photoelectron experiments and theoretical computations. *Chem. Rev.* 102:231–82
14. Simons J. 2008. Molecular anions. *J. Phys. Chem. A* 112:6401–511
15. Lineberger WC. 2013. Once upon anion: a tale of photodetachment. *Annu. Rev. Phys. Chem.* 64:21–36
16. Ellison GB, Engelking PC, Lineberger WC. 1978. An experimental determination of the geometry and electron affinity of CH_3. *J. Am. Chem. Soc.* 100:2556–58
17. Ramond TM, Davico GE, Schwartz RL, Lineberger WC. 2000. Vibronic structure of alkoxy radicals via photoelectron spectroscopy. *J. Chem. Phys.* 112:1158–69
18. Ichino T, Wren SW, Vogelhuber KM, Gianola AJ, Lineberger WC, Stanton JF. 2008. The vibronic level structure of the cyclopentadienyl radical. *J. Chem. Phys.* 129:084310
19. Wang X-B, Fu QA, Yang J. 2010. Electron affinities and electronic structures of *o*-, *m*-, and *p*-hydroxyphenoxyl radicals: a combined low-temperature photoelectron spectroscopic and *ab initio* calculation study. *J. Phys. Chem. A* 114:9083–89
20. Leopold DG, Ho J, Lineberger WC. 1987. Photoelectron spectroscopy of mass-selected metal cluster anions. I. Cu_n^-, $n = 1$–10. *J. Chem. Phys.* 86:1715–26
21. Coe JV, Lee GH, Eaton JG, Arnold ST, Sarkas HW, et al. 1990. Photoelectron spectroscopy of hydrated electron cluster anions, $(H_2O)^-_{n\ =\ 2–69}$. *J. Chem. Phys.* 92:3980–82
22. Castleman AW, Bowen KH. 1996. Clusters: structure, energetics, and dynamics of intermediate states of matter. *J. Phys. Chem.* 100:12911–44
23. Zhai H-J, Wang L-S. 2007. Probing the electronic structure and band gap evolution of titanium oxide clusters $(TiO_2)_n^-$ ($n = 1$–10) using photoelectron spectroscopy. *J. Am. Chem. Soc.* 129:3022–26
24. Bartels C, Hock C, Huwer J, Kuhnen R, Schwöbel J, von Issendorff B. 2009. Probing the angular momentum character of the valence orbitals of free sodium nanoclusters. *Science* 323:1323–27
25. Wenthold PG, Hrovat DA, Borden WT, Lineberger WC. 1996. Transition-state spectroscopy of cyclooctatetraene. *Science* 272:1456–59
26. Neumark DM. 2005. Probing the transition state with negative ion photodetachment: experiment and theory. *Phys. Chem. Chem. Phys.* 7:433–42
27. Celotta RJ, Bennett RA, Hall JL, Siegel MW, Levine J. 1972. Molecular photodetachment spectrometry. II. Electron affinity of O_2 and structure of O_2^-. *Phys. Rev. A* 6:631–42
28. Leopold DG, Murray KK, Miller AES, Lineberger WC. 1985. Methylene: a study of the $X\,^3B_1$ and $a\,^1a_1$ states by photoelectron spectroscopy of CH_2^- and CD_2^-. *J. Chem. Phys.* 83:4849–65
29. Ervin KM, Lineberger WC. 1991. Photoelectron spectra of C_2^- and C_2H^-. *J. Phys. Chem.* 95:1167–77
30. Weaver A, Arnold DW, Bradforth SE, Neumark DM. 1991. Examination of the $^2A'_2$ and $^2E'$ states of NO_3 by ultraviolet photoelectron spectroscopy of NO_3^-. *J. Chem. Phys.* 94:1740–51
31. Simons J. 1981. Propensity rules for vibration-induced electron detachment of anions. *J. Am. Chem. Soc.* 103:3971–76
32. Osterwalder A, Nee MJ, Zhou J, Neumark DM. 2004. High resolution photodetachment spectroscopy of negative ions via slow photoelectron imaging. *J. Chem. Phys.* 121:6317–22
33. Neumark DM. 2008. Slow electron velocity-map imaging of negative ions: applications to spectroscopy and dynamics. *J. Phys. Chem. A* 112:13287–301
34. Hock C, Kim JB, Weichman ML, Yacovitch TI, Neumark DM. 2012. Slow photoelectron velocity-map imaging spectroscopy of cold negative ions. *J. Chem. Phys.* 137:244201
35. Brehm B, Gusinow MA, Hall JL. 1967. Electron affinity of helium via laser photodetachment of its negative ion. *Phys. Rev. Lett.* 19:737–41
36. Posey LA, Deluca MJ, Johnson MA. 1986. Demonstration of a pulsed photoelectron spectrometer on mass-selected negative ions: O^-, O_2^-, and O_4^-. *Chem. Phys. Lett.* 131:170–74
37. Cheshnovsky O, Yang SH, Pettiette CL, Craycraft MJ, Liu Y, Smalley RE. 1987. Ultraviolet photoelectron spectroscopy of semiconductor clusters: silicon and germanium. *Chem. Phys. Lett.* 138:119–24
38. Kruit P, Read FH. 1983. Magnetic-field parallelizer for 2π electron-spectrometer and electron-image magnifier. *J. Phys. E* 16:313–24

39. Chandler DW, Houston PL. 1987. Two-dimensional imaging of state-selected photodissociation products detected by multiphoton ionization. *J. Chem. Phys.* 87:1445–47
40. Eppink ATJB, Parker DH. 1997. Velocity-map imaging of ions and electrons using electrostatic lenses: application in photoelectron and photofragment ion imaging of molecular oxygen. *Rev. Sci. Instrum.* 68:3477–84
41. Baguenard B, Pinaré JC, Bordas C, Broyer M. 2001. Photoelectron imaging spectroscopy of small tungsten clusters: direct observation of thermionic emission. *Phys. Rev. A* 63:023204
42. Surber E, Mabbs R, Sanov A. 2003. Probing the electronic structure of small molecular anions by photoelectron imaging. *J. Phys. Chem. A* 107:8215–24
43. Suzuki T, Whitaker BJ. 2001. Non-adiabatic effects in chemistry revealed by time-resolved charged-particle imaging. *Int. Rev. Phys. Chem.* 20:313–56
44. Stolow A, Bragg AE, Neumark DM. 2004. Femtosecond time-resolved photoelectron spectroscopy. *Chem. Rev.* 104:1719–57
45. Metz RB, Weaver A, Bradforth SE, Kitsopoulos TN, Neumark DM. 1990. Probing the transition state with negative ion photodetachment: the Cl + HCl and Br + HBr reactions. *J. Phys. Chem.* 94:1377–88
46. Wang L-S, Cheng H-S, Fan JW. 1995. Photoelectron spectroscopy of size-selected transition metal clusters: Fe_n^-, $n = 3$–24. *J. Chem. Phys.* 102:9480–93
47. Müller-Dethlefs K, Sander M, Schlag EW. 1984. Two-colour photoionization resonance spectroscopy of NO: complete separation of rotational levels of NO^+ at the ionization threshold. *Chem. Phys. Lett.* 112:291–94
48. Müller-Dethlefs K, Schlag EW. 1991. High-resolution zero kinetic energy (ZEKE) photoelectron spectroscopy of molecular systems. *Annu. Rev. Phys. Chem.* 42:109–36
49. Kitsopoulos TN, Waller IM, Loeser JG, Neumark DM. 1989. High-resolution threshold photodetachment spectroscopy of negative ions. *Chem. Phys. Lett.* 159:300–6
50. Lenzer T, Yourshaw I, Furlanetto MR, Reiser G, Neumark DM. 1999. Zero electron kinetic energy spectroscopy of the $ArCl^-$ anion. *J. Chem. Phys.* 110:9578–86
51. Reiser G, Müller-Dethlefs K. 1992. Rotationally resolved zero kinetic energy photoelectron spectroscopy of nitric oxide. *J. Phys. Chem.* 96:9–12
52. Arnold CC, Neumark DM. 1993. Study of Si_4 and Si_4^- using threshold photodetachment (ZEKE) spectroscopy. *J. Chem. Phys.* 99:3353–62
53. Waller IM, Kitsopoulos TN, Neumark DM. 1990. Threshold photodetachment spectroscopy of the I + HI transition state region. *J. Phys. Chem.* 94:2240–42
54. Arnold CC, Neumark DM. 1995. Study of small carbon and silicon clusters using negative ion photodetachment techniques. In *Advances in Metal and Semiconductor Clusters*, ed. MA Duncan, pp. 113–48. Greenwich, CT: JAI Press
55. Arnold CC, Neumark DM, Cyr DM, Johnson MA. 1995. Negative ion zero electron kinetic energy spectroscopy of I^-CH_3I. *J. Phys. Chem.* 99:1633–36
56. Burton GR, Xu CS, Arnold CC, Neumark DM. 1996. Photoelectron spectroscopy and zero electron kinetic energy spectroscopy of germanium cluster anions. *J. Chem. Phys.* 104:2757–64
57. Lenzer T, Furlanetto MR, Pivonka NL, Neumark DM. 1999. Zero electron kinetic energy and threshold photodetachment spectroscopy of Xe_nI^- clusters ($n = 2$–14): binding, many-body effects, and structures. *J. Chem. Phys.* 110:6714–31
58. Blondel C, Delsart C, Dulieu F. 1996. The photodetachment microscope. *Phys. Rev. Lett.* 77:3755–58
59. Valli C, Blondel C, Delsart C. 1999. Measuring electron affinities with the photodetachment microscope. *Phys. Rev. A* 59:3809–15
60. Delsart C, Goldfarb F, Blondel C. 2002. Molecular photodetachment microscopy. *Phys. Rev. Lett.* 89:183002
61. Cavanagh SJ, Gibson ST, Gale MN, Dedman CJ, Roberts EH, Lewis BR. 2007. High-resolution velocity-map-imaging photoelectron spectroscopy of the O^- photodetachment fine-structure transitions. *Phys. Rev. A* 76:052708
62. León I, Yang Z, Liu HT, Wang L-S. 2014. The design and construction of a high-resolution velocity-map imaging apparatus for photoelectron spectroscopy studies of size-selected clusters. *Rev. Sci. Instrum.* 85:083106

63. Harrison AW, Ryazanov M, Sullivan EN, Neumark DM. 2016. Photodissociation dynamics of the methyl perthiyl radical at 248 and 193 nm using fast-beam photofragment translational spectroscopy. *J. Chem. Phys.* 145:024305
64. Weichman ML, DeVine JA, Levine DS, Kim JB, Neumark DM. 2016. Isomer-specific vibronic structure of the 9-, 1-, and 2-anthracenyl radicals via slow photoelectron velocity-map imaging. *PNAS* 113:1698–705
65. Gerlich D. 1992. Inhomogeneous RF fields: a versatile tool for the study of processes with slow ions. In *State-Selected and State-to-State Ion–Molecule Reaction Dynamics, Part 1: Experiment*, ed. C-Y Ng, M Baer, I Prigogine, SA Rice, pp. 1–176. New York: Wiley
66. Wester R. 2009. Radiofrequency multipole traps: tools for spectroscopy and dynamics of cold molecular ions. *J. Phys. B* 42:154001
67. Campbell WC, Doyle JM. 2009. Cooling, trap loading, and beam production using a cryogenic helium buffer gas. In *Cold Molecules: Theory, Experiment, Applications*, ed. R Krems, WC Stwalley, B Friedrich, pp. 473–508. Boca Raton, FL: CRC Press
68. Luo ZH, Chen XL, Li JM, Ning CG. 2016. Precision measurement of the electron affinity of niobium. *Phys. Rev. A* 93:020501(R)
69. Wang L-S. 2015. Electrospray photoelectron spectroscopy: from multiply-charged anions to ultracold anions. *J. Chem. Phys.* 143:040901
70. Zhu G-Z, Huang D-L, Wang L-S. 2017. Conformation-selective resonant photoelectron imaging from dipole-bound states of cold 3-hydroxyphenoxide. *J. Chem. Phys.* 147:013910
71. Bartels C, Hock C, Kuhnen R, von Issendorff B. 2014. Photoelectron imaging spectroscopy of the small sodium cluster anions Na_3^-, Na_5^-, and Na_7^-. *J. Phys. Chem. A* 118:8270–76
72. Li H-F, Zhao Y-X, Yuan Z, Liu Q-Y, Li Z-Y, et al. 2017. Methane activation by tantalum carbide cluster anions $Ta_2C_4^-$. *J. Phys. Chem. Lett.* 8:605–10
73. Mascaritolo KJ, Dermer AR, Green ML, Gardner AM, Heaven MC. 2017. Photodetachment spectroscopy of the beryllium oxide anion, BeO^-. *J. Chem. Phys.* 146:054301
74. Kregel SJ, Thurston GK, Zhou J, Garand E. 2017. A multi-plate velocity-map imaging design for high-resolution photoelectron spectroscopy. *J. Chem. Phys.* 147:094201
75. Oliveira AM, Lu Y-J, Lehman JH, Changala PB, Baraban JH, et al. 2015. Photoelectron spectroscopy of the methide anion: electron affinities of $\bullet CH_3$ and $\bullet CD_3$ and inversion splittings of CH_3^- and CD_3^-. *J. Am. Chem. Soc.* 137:12939–45
76. Nelson DJ, Gichuhi WK, Miller EM, Lehman JH, Lineberger WC. 2017. Anion photoelectron spectroscopy of deprotonated *ortho*-, *meta*-, and *para*-methylphenol. *J. Chem. Phys.* 146:074302
77. Culberson LM, Blackstone CC, Wallace AA, Sanov A. 2015. Aromatic stabilization and hybridization trends in photoelectron imaging of heterocyclic radicals and anions. *J. Phys. Chem. A* 119:9770–77
78. Cavanagh SJ, Gibson ST, Lewis BR. 2012. High-resolution photoelectron spectroscopy of linear ← bent polyatomic photodetachment transitions: the electron affinity of CS_2. *J. Chem. Phys.* 137:144304
79. Applegate BE, Barckholtz TA, Miller TA. 2003. Explorations of conical intersections and their ramifications for chemistry through the Jahn–Teller effect. *Chem. Soc. Rev.* 32:38–49
80. Miller TA. 2006. Spectroscopic probing and diagnostics of the geometric structure of the alkoxy and alkyl peroxy radical intermediates. *Mol. Phys.* 104:2581–93
81. Kim JB, Weichman ML, Yacovitch TI, Shih C, Neumark DM. 2013. Slow photoelectron velocity-map imaging spectroscopy of the C_9H_7 (indenyl) and $C_{13}H_9$ (fluorenyl) anions. *J. Chem. Phys.* 139:104301
82. Weichman ML, Kim JB, DeVine JA, Levine DS, Neumark DM. 2015. Vibrational and electronic structure of the α- and β-naphthyl radicals via slow photoelectron velocity-map imaging. *J. Am. Chem. Soc.* 137:1420–23
83. Ervin KM, Ramond TM, Davico GE, Schwartz RL, Casey SM, Lineberger WC. 2001. Naphthyl radical: negative ion photoelectron spectroscopy, Franck–Condon simulation, and thermochemistry. *J. Phys. Chem. A* 105:10822–31
84. Richter H, Howard JB. 2000. Formation of polycyclic aromatic hydrocarbons and their growth to soot—a review of chemical reaction pathways. *Prog. Energy Combust. Sci.* 26:565–608
85. Tielens AGGM. 2008. Interstellar polycyclic aromatic hydrocarbon molecules. *Annu. Rev. Astron. Astrophys.* 46:289–337

86. DePuy CH, Bierbaum VM, Flippin LA, Grabowski JJ, King GK, et al. 1980. Gas-phase reactions of anions with substituted silanes. *J. Am. Chem. Soc.* 102:5012–15
87. Zhou J, Garand E, Eisfeld W, Neumark DM. 2007. Slow electron velocity-map imaging spectroscopy of the 1-propynyl radical. *J. Chem. Phys.* 127:034304
88. DeVine JA, Weichman ML, Lyle SJ, Neumark DM. 2017. High-resolution photoelectron imaging of cryogenically cooled α- and β-furanyl anions. *J. Mol. Spectrosc.* 332:16–21
89. Lykke KR, Murray KK, Neumark DM, Lineberger WC. 1988. High-resolution studies of autodetachment in negative ions. *Phil. Trans. R. Soc. A* 324:179–96
90. Liu H-T, Ning C-G, Huang D-L, Dau PD, Wang L-S. 2013. Observation of mode-specific vibrational autodetachment from dipole-bound states of cold anions. *Angew. Chem. Int. Ed.* 52:8976–79
91. Huang D-L, Liu H-T, Ning C-G, Wang L-S. 2015. Vibrational state-selective autodetachment photoelectron spectroscopy from dipole-bound states of cold 2-hydroxyphenoxide: *o*-$HO(C_6H_4)O^-$. *J. Chem. Phys.* 142:124309
92. Liu H-T, Ning C-G, Huang D-L, Wang L-S. 2014. Vibrational spectroscopy of the dehydrogenated uracil radical by autodetachment of dipole-bound excited states of cold anions. *Angew. Chem. Int. Ed.* 53:2464–68
93. Huang D-L, Liu H-T, Ning C-G, Dau PD, Wang L-S. 2017. Resonant photoelectron imaging of deprotonated uracil anion via vibrational levels of a dipole-bound excited state. *Chem. Phys.* 482:374–83
94. Huang D-L, Liu H-T, Ning C-G, Zhu G-Z, Wang L-S. 2015. Probing the vibrational spectroscopy of the deprotonated thymine radical by photodetachment and state-selective autodetachment photoelectron spectroscopy via dipole-bound states. *Chem. Sci.* 6:3129–38
95. Huang D-L, Zhu G-Z, Liu Y, Wang L-S. 2017. Photodetachment spectroscopy and resonant photoelectron imaging of cryogenically-cooled deprotonated 2-hydroxypyrimidine anions. *J. Mol. Spectrosc.* 332:86–93
96. Huang D-L, Liu H-T, Ning C-G, Wang L-S. 2015. Conformation-selective resonant photoelectron spectroscopy via dipole-bound states of cold anions. *J. Phys. Chem. Lett.* 6:2153–57
97. Bell AT, Head-Gordon M. 2011. Quantum mechanical modeling of catalytic processes. *Annu. Rev. Chem. Biomol. Eng.* 2:453–77
98. Zemski KA, Justes DR, Castleman AW. 2002. Studies of metal oxide clusters: elucidating reactive sites responsible for the activity of transition metal oxide catalysts. *J. Phys. Chem. B* 106:6136–48
99. Johnson GE, Mitrić R, Bonačić-Koutecký V, Castleman AW. 2009. Clusters as model systems for investigating nanoscale oxidation catalysis. *Chem. Phys. Lett.* 475:1–9
100. Sauer J, Freund HJ. 2015. Models in catalysis. *Catal. Lett.* 145:109–25
101. Kim JB, Weichman ML, Neumark DM. 2014. Slow photoelectron velocity-map imaging spectroscopy of the Fe_3O^- and Co_3O^- anions. *J. Chem. Phys.* 141:174307
102. Weichman ML, DeVine JA, Neumark DM. 2016. High-resolution photoelectron imaging spectroscopy of cryogenically cooled Fe_4O^- and Fe_5O^-. *J. Chem. Phys.* 145:054302
103. Kim JB, Weichman ML, Neumark DM. 2015. Low-lying states of FeO and FeO^- by slow photoelectron spectroscopy. *Mol. Phys.* 113:2105–14
104. Kim JB, Weichman ML, Neumark DM. 2014. Vibronic structure of VO_2 probed by slow photoelectron velocity-map imaging spectroscopy. *J. Chem. Phys.* 140:034307
105. Gong Y, Zhou MF, Andrews L. 2009. Spectroscopic and theoretical studies of transition metal oxides and dioxygen complexes. *Chem. Rev.* 109:6765–808
106. Asmis KR. 2012. Structure characterization of metal oxide clusters by vibrational spectroscopy: possibilities and prospects. *Phys. Chem. Chem. Phys.* 14:9270–81
107. Duncan MA. 2012. Laser vaporization cluster sources. *Rev. Sci. Instrum.* 83:041101
108. Wang L-S, Li X, Zhang H-F. 2000. Probing the electronic structure of iron clusters using photoelectron spectroscopy. *Chem. Phys.* 262:53–63
109. Kim JB, Weichman ML, Neumark DM. 2014. Structural isomers of Ti_2O_4 and Zr_2O_4 anions identified by slow photoelectron velocity-map imaging spectroscopy. *J. Am. Chem. Soc.* 136:7159–68
110. Wu H, Wang L-S. 1997. Electronic structure of titanium oxide clusters: TiO_y ($y = 1$–3) and $(TiO_2)_n$ ($n = 1$–4). *J. Chem. Phys.* 107:8221–28

111. Li SG, Dixon DA. 2008. Molecular structures and energetics of the $(TiO_2)_n$ (n = 1–4) clusters and their anions. *J. Phys. Chem. A* 112:6646–66
112. Li SG, Dixon DA. 2010. Molecular structures and energetics of the $(ZrO_2)_n$ and $(HfO_2)_n$ (n = 1–4) clusters and their anions. *J. Phys. Chem. A* 114:2665–83
113. Ramabhadran RO, Mann JE, Waller SE, Rothgeb DW, Jarrold CC, Raghavachari K. 2013. New insights on photocatalytic H_2 liberation from water using transition-metal oxides: lessons from cluster models of molybdenum and tungsten oxides. *J. Am. Chem. Soc.* 135:17039–51
114. Daniel MC, Astruc D. 2004. Gold nanoparticles: assembly, supramolecular chemistry, quantum-size-related properties, and applications toward biology, catalysis, and nanotechnology. *Chem. Rev.* 104:293–346
115. Wang L-M, Wang L-S. 2012. Probing the electronic properties and structural evolution of anionic gold clusters in the gas phase. *Nanoscale* 4:4038–53
116. Pande S, Huang W, Shao N, Wang L-M, Khetrapal N, et al. 2016. Structural evolution of core-shell gold nanoclusters: Au_n^- (n = 42–50). *ACS Nano* 10:10013–22
117. Khetrapal NS, Jian T, Pal R, Lopez GV, Pande S, et al. 2016. Probing the structures of gold-aluminum alloy clusters $Au_xAl_y^-$: a joint experimental and theoretical study. *Nanoscale* 8:9805–14
118. Yang Z, Leon I, Wang L-S. 2013. Vibrational spectroscopy of Au_4 from high resolution photoelectron imaging. *J. Chem. Phys.* 139:021106
119. Lopez GV, Czekner J, Jian T, Li W-L, Yang Z, Wang L-S. 2014. Probing the electronic and vibrational structure of $Au_2Al_2^-$ and Au_2Al_2 using photoelectron spectroscopy and high resolution photoelectron imaging. *J. Chem. Phys.* 141:224309
120. Handschuh H, Ganteför G, Eberhardt W. 1995. Vibrational spectroscopy of clusters using a "magnetic bottle" electron spectrometer. *Rev. Sci. Instrum.* 66:3838–43
121. Häkkinen H, Yoon B, Landman U, Li X, Zhai H-J, Wang L-S. 2003. On the electronic and atomic structures of small Au_N^- (N = 4–14) clusters: a photoelectron spectroscopy and density-functional study. *J. Phys. Chem. A* 107:6168–75
122. Furche F, Ahlrichs R, Weis P, Jacob C, Gilb S, et al. 2002. The structures of small gold cluster anions as determined by a combination of ion mobility measurements and density functional calculations. *J. Chem. Phys.* 117:6982–90
123. Gao Y, Zhao Y, Zeng XC. 2010. Reexamination of low energy structures of Au_4^- and Au_4. *J. Theor. Comput. Chem.* 9:1–7
124. Häkkinen H, Moseler M, Landman U. 2002. Bonding in Cu, Ag, and Au clusters: relativistic effects, trends, and surprises. *Phys. Rev. Lett.* 89:033401
125. Jacobson MP, Field RW. 2000. Acetylene at the threshold of isomerization. *J. Phys. Chem. A* 104:3073–86
126. Gerardi HK, Breen KJ, Guasco TL, Weddle GH, Gardenier GH, et al. 2010. Survey of Ar-tagged predissociation and vibrationally mediated photodetachment spectroscopies of the vinylidene anion, $C_2H_2^-$. *J. Phys. Chem. A* 114:1592–601
127. Ervin KM, Ho J, Lineberger WC. 1989. A study of the singlet and triplet states of vinylidene by photoelectron spectroscopy of $H_2C{=}C^-$, $D_2C{=}C^-$, and $HDC{=}C^-$. Vinylidene-acetylene isomerization. *J. Chem. Phys.* 91:5974–92
128. Carrington T Jr., Hubbard LM, Schaefer HF III, Miller WH. 1984. Vinylidene: potential energy surface and unimolecular reaction dynamics. *J. Chem. Phys.* 80:4347–54
129. DeVine JA, Weichman ML, Zhou X, Ma J, Jiang B, et al. 2016. Non-adiabatic effects on excited states of vinylidene observed with slow photoelectron velocity-map imaging. *J. Am. Chem. Soc.* 138:16417–25
130. Stanton JF, Gauss J. 1994. Some predictions relevant to future spectroscopic observation of S_1 vinylidene. *J. Chem. Phys.* 101:3001–5
131. DeVine JA, Weichman ML, Laws B, Chang J, Babin MC, et al. 2017. Encoding of vinylidene isomerization in its anion photoelectron spectrum. *Science* 20:336–39
132. Polanyi JC, Zewail AH. 1995. Direct observation of the transition state. *Acc. Chem. Res.* 28:119–32
133. Neumark DM, Wodtke AM, Robinson GN, Hayden CC, Lee YT. 1985. Molecular beam studies of the $F + H_2$ reaction. *J. Chem. Phys.* 82:3045–66
134. Skodje RT, Skouteris D, Manolopoulos DE, Lee S-H, Dong F, Liu K. 2000. Observation of a transition state resonance in the integral cross section of the F + HD reaction. *J. Chem. Phys.* 112:4536–52

135. Qiu M, Ren Z, Che L, Dai D, Harich SA, et al. 2006. Observation of Feshbach resonances in the F + H_2 → HF + H reaction. *Science* 311:1440–43
136. Manolopoulos DE, Stark K, Werner H-J, Arnold DW, Bradforth SE, Neumark DM. 1993. The transition state of the F + H_2 reaction. *Science* 262:1852–55
137. Russell CL, Manolopoulos DE. 1996. How to observe the elusive resonances in F + H_2 reactive scattering. *Chem. Phys. Lett.* 256:465–73
138. Yacovitch TI, Garand E, Kim JB, Hock C, Theis T, Neumark DM. 2012. Vibrationally resolved transition state spectroscopy of the F + H_2 and F + CH_4 reactions. *Faraday Disc*. 157:399–414
139. Kim JB, Weichman ML, Sjolander TF, Neumark DM, Klos J, et al. 2015. Spectroscopic observation of resonances in the F + H_2 reaction. *Science* 349:510–13
140. Lique F, Li GL, Werner HJ, Alexander MH. 2011. Non-adiabatic coupling and resonances in the F + H_2 reaction at low energies. *J. Chem. Phys.* 134:231101
141. Weichman ML, DeVine JA, Babin MC, Li J, Guo L, et al. 2017. Feshbach resonances in the exit channel of the F + CH_3OH → HF + CH_3O reaction observed using transition-state spectroscopy. *Nat. Chem.* 9:950–55
142. Bradforth SE, Arnold DW, Metz RB, Weaver A, Neumark DM. 1991. Spectroscopy of the transition state: hydrogen abstraction reactions of fluorine. *J. Phys. Chem.* 95:8066–78
143. Ray AW, Agarwal J, Shen BB, Schaefer HF, Continetti RE. 2016. Energetics and transition-state dynamics of the F + $HOCH_3$ → HF + OCH_3 reaction. *Phys. Chem. Chem. Phys.* 18:30612–21
144. Geusic ME, Morse MD, O'Brien SC, Smalley RE. 1985. Surface reactions of metal clusters I: the fast flow cluster reactor. *Rev. Sci. Instrum.* 56:2123–30
145. Kemper PR, Dupuis NF, Bowers MT. 2009. A new, higher resolution, ion mobility mass spectrometer. *Int. J. Mass Spectrom.* 287:46–57